EcoEnergy

WILEY

EcoEnergy

RESEARCH ARTICLE OPEN ACCESS

Defect-Engineered Nested Metallic Cu Clusters Enhance CO_2 Photoreduction in Photothermal 2D Plasmonic CuSe

Huaipeng Pang[1] | Janobiddinkhuja Bahodurov[2] | Tianxi Zhang[2] | Minmin Gao[3] | Weili Ong[3] | Sergey M. Kozlov[2] | Fan Lu Meng[1] | Ghim Wei Ho[3,4]

[1]School of Materials Science and Engineering, Ocean University of China, Qingdao, China | [2]Department of Chemical & Biomolecular Engineering, National University of Singapore, 4 Engineering Drive 4, Singapore | [3]Department of Electrical and Computer Engineering, National University of Singapore, 4 Engineering Drive 3, Singapore | [4]Department of Materials Science and Engineering, National University of Singapore, 9 Engineering Drive 1, Singapore

Correspondence: Fan Lu Meng (mengfanlu@ouc.edu.cn) | Sergey M. Kozlov (sergey.kozlov@nus.edu.sg) | Ghim Wei Ho (elehgw@nus.edu.sg)

Received: 20 June 2025 | **Revised:** 14 January 2026 | **Accepted:** 27 January 2026

Keywords: CO_2 reduction | photocatalyst | photothermal | plasmonic CuSe | Se vacancy

ABSTRACT

Photocatalytic CO_2 conversion driven by solar energy offers a sustainable pathway for carbon neutrality, but remains limited by inefficient charge dynamics and poor spectral utilization. However, copper chalcogenides exhibit dual UV–vis absorption and near-infrared (NIR) plasmonic resonance suffer from rapid electron–hole recombination and insufficient catalytic activity. This study introduces nested metallic-semiconductor Cu-based heterostructures (Cu/CuSe) synthesized through dissolution–reduction to address these limitations. The engineered architecture incorporates metallic Cu clusters and selenium vacancies within CuSe nanosheets, which collectively broaden NIR absorption through defect-induced gap states for enhanced photothermal activation. This approach promotes directional electron transfer to Cu clusters, which suppress electron–hole recombination and serve as catalytically active sites. Additionally, seamless coupling between the components lowers interfacial energy losses. Density functional theory calculations reveal that Cu clusters effectively reduce CO_2 activation barriers by stabilizing critical reaction intermediates. The heterostructures achieve a threefold increase in CO yield (27.06 μmol g^{-1} h^{-1}) under full-spectrum irradiation compared to pristine CuSe, with a 90% selectivity without sacrificial agents. The photothermal–photocatalytic synergy harnesses a cascade energy conversion pathway, outperforming conventional plasmonic semiconductor systems. This work establishes a defect-engineering strategy to enhance infrared energy harvesting and charge management in broadband-responsive photocatalysts.

1 | Introduction

Photocatalytic CO_2 reduction driven by renewable sunlight is a highly sought-after strategy among feasible pathways for green fuel production. [1–5] However, the CO_2 reduction process is bound by sluggish kinetics owing to the inherent chemical inertness of C=O bond and the complexity of multiple proton-coupled electron transfer steps. Consequently, the energetic photogenerated charge carrier is of paramount importance to activate CO_2 molecules and trigger the reaction progression by overcoming these barriers. [6–10] A variety of strategies of the design of effective CO_2 reduction photocatalysts have been developed to address these challenges, such as tuning the energy band configuration of semiconductor photocatalysts to ensure sufficient redox potential from photoexcited electrons and holes, [11–14] and geometric engineering of plasmonic photocatalysts for intensive localized surface plasmon resonance (LSPR) to achieve copious hot electrons with favorable energy potential. [15–18] Furthermore, hybrid systems enhanced by coupling plasmonic noble metals with semiconductors have been proposed to synergistically utilize a broader UV–visible (UV–vis) spectrum. [19–23] Various combinations of metals and semiconductors can produce distinct optical responses and generate hot electrons, which either cross the Schottky barrier at the

semiconductor–metal interface to directly participate in the reaction or supply thermal energy to the surrounding. [24–26] However, inefficient hot charge carrier transfer and minimal infrared (IR) light absorption still limit the overall solar energy conversion efficiency [27].

Plasmonic semiconductors, for example, copper chalcogenides (CuSe, $Cu_{2-x}Se$, CuS, etc.) uniquely present Schottky barrier-free hybrids owing to their exquisite electronic structures and optical properties that can produce photo-generated electron–hole pairs under UV–vis light irradiation while simultaneously exhibit LSPR property in the NIR region. [28–31] Although this broad-spectrum absorption is highly conducive to superior solar energy conversion, it does not necessarily translate into strong CO_2 reduction capabilities. One key limitation is the rapid electron–hole recombination, poor charge migration capability and feeble charge carriers dynamics associated to their narrow band gaps. [32, 33] Besides, the limited LSPR excitation at longer plasmonic resonance wavelength leads to low concentrations of hot charge carriers with insufficient energy potential, which are inadequate for directly catalyzing the transformation of adsorbed molecules. [34] Instead, the plasmonic excitation primarily contributes to photothermal heating, lowering activation energy and accelerating the photocatalytic process. To address these issues, it is crucial to expand the IR absorption of copper chalcogenides for enhanced photothermal effect, promote efficient separation and transfer of photoexcited electron–hole pairs, and introduce highly active sites for CO_2 reduction.

Herein, we propose a nested Cu-based heterostructure, Cu/CuSe, synthesized through a dissolution and partial re-reduction that simultaneously create in-plane metallic Cu clusters and Se vacancies that are embedded within CuSe nanosheets. The nested Cu cluster network in Cu/CuSe nanosheets is tailored to efficiently extend photothermal conversion beyond the innate plasmonic properties through defects-induced disorder and new gap states arising from anion site vacancies (Figure 1). These vacancies broaden photon absorption, whereas the laterally embedded metallic Cu clusters capture photoelectrons to suppress rapid electron–hole recombination and act as key catalytic centers for CO_2 reduction, as validated by density functional theory (DFT) calculations and experimental characterization. Besides, the seamless coupling of Cu, CuSe, and Se vacancies built-in within the nanosheet matrix shortens the charge carrier transport length and lowers interfacial energy losses. Consequently, the Cu/CuSe heterostructures reveals enhanced activity and selectivity toward photocatalytic CO_2 reduction under UV–vis irradiation compared to pure plasmonic CuSe. A nearly threefold increase in CO yield rate is achieved upon photothermal activation, triggering photo-redox conversion of CO_2 under full solar spectrum without the use of sacrificial agents and photosensitizers. This work demonstrates a facile approach to expand infrared light-responsiveness in plasmonic semiconductors, offering a promising route to facilitate high-efficiency sustainable photocatalytic reactions.

2 | Results and Discussion

Pristine CuSe nanosheets were prepared using a co-precipitation method. Subsequently, partial dissolution of anions and localized re-reduction under ultrasonic treatment gradually generated Se vacancies and in-plane metallic Cu clusters to form Cu/CuSe upon the re-addition of $NaBH_4$ agent, as illustrated in the schematic diagram (Figure 2a). The scanning electron microscopy (SEM) (Figure 2b), transmission electron microscopy (TEM) (Figure 2c), selected area electron diffraction (SAED) images (Supporting Information S1: Figure S1), and X-ray diffraction (XRD) patterns (Supporting Information S1: Figure S3) confirm the formation of hexagonal phase CuSe with a nanosheet morphology. After post-processing, the Cu/CuSe nanosheets exhibit a slightly rougher surface compared to the incipient one, with the appearance of distinct nanopores (Figure 2d). The average sheet thickness of Cu/CuSe was determined to be approximately 4.1 nm using atomic force microscopy (AFM) (Figure 2h,i), which is similar to that of pristine CuSe (Supporting Information S1: Figure S2). Despite the introduction of defects, the Cu/CuSe preserves the original sheet-like structure. XRD analysis is further performed to

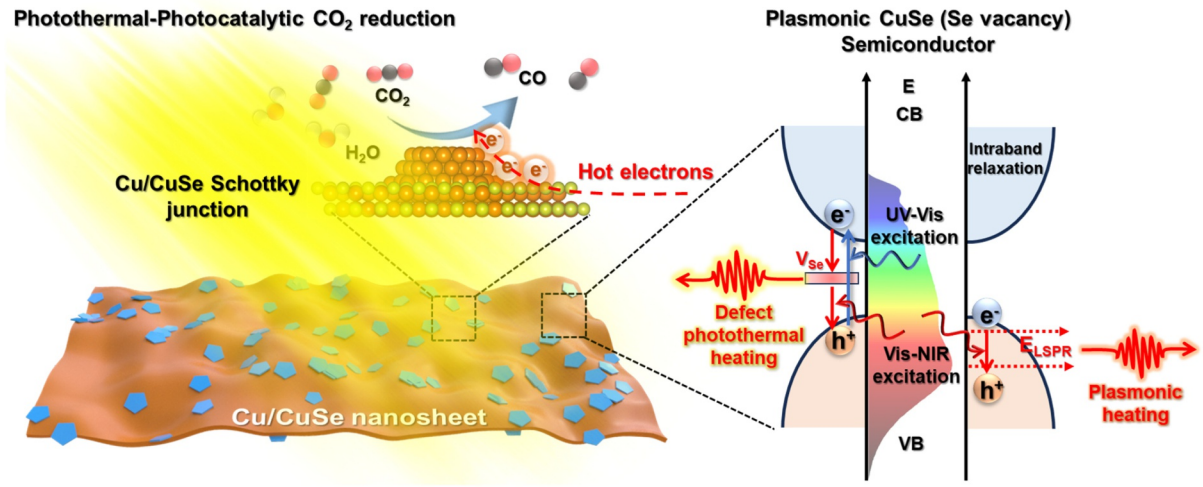

FIGURE 1 | Schematic drawing of the photothermal–photocatalytic CO_2 reduction in 2D Plasmonic CuSe featuring a Cu/CuSe Schottky junction and Se vacancies.

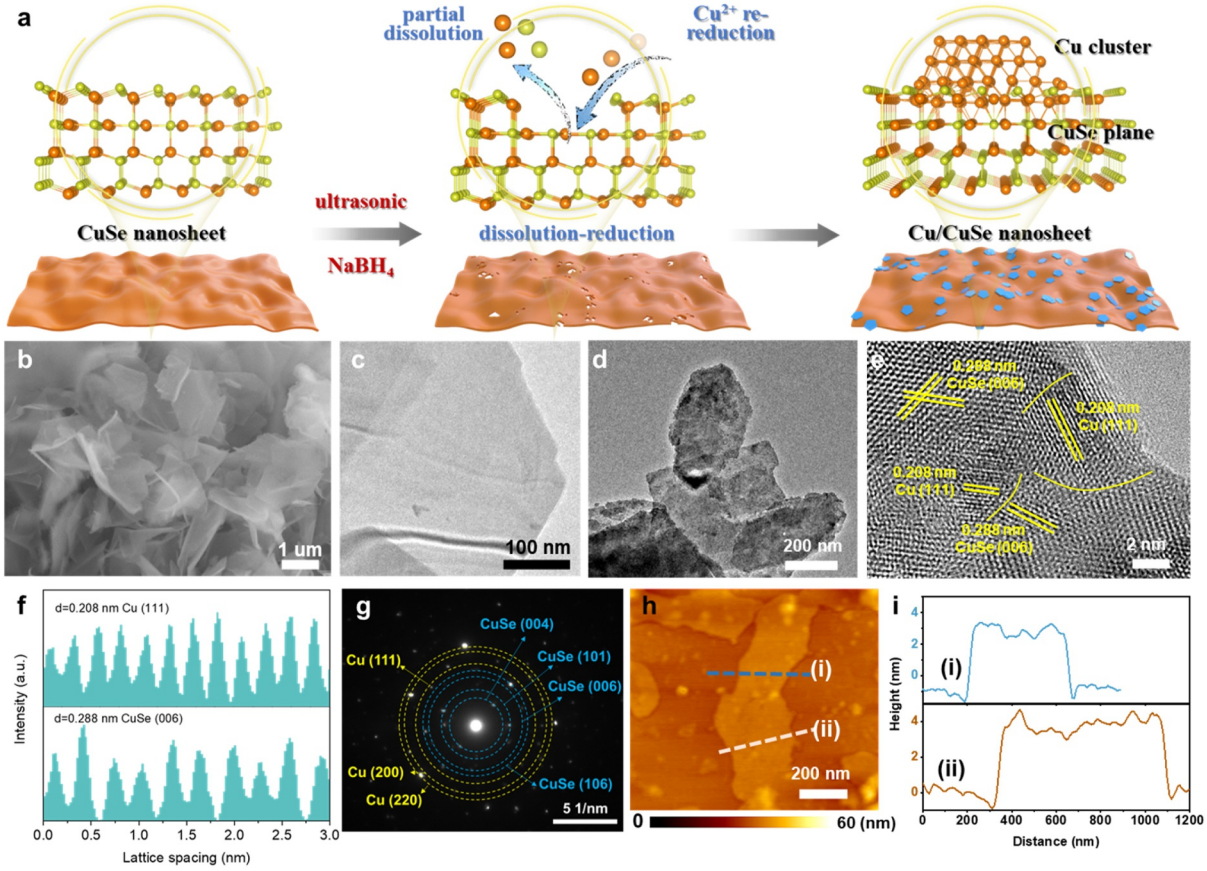

FIGURE 2 | (a) Schematic diagram of the nested metallic Cu centers in 2D plasmonic CuSe (Cu/CuSe). SEM (b) and TEM (c) image of CuSe. TEM (d) and HRTEM (e) images of Cu/CuSe. Lattice spacing (f) and SAED image (g) of Cu/CuSe. (h) AFM image and relative thickness (i) along the lines marked on panel h.

investigate the structural evolution of the sample. A reduction in the intensity of the (006) peak of Cu/CuSe (Supporting Information S1: Figure S3) indicates microstructural modification. [34–36] Notably, no diffraction peaks assigned to Cu metal are detected, which suggests that the metallic Cu exists at low concentrations and in a dispersed state, which is further verified by high-resolution TEM (HRTEM) imaging. The HRTEM images (Figure 2e) of Cu/CuSe, measured interplanar spacings (Figure 2f), and the corresponding SAED pattern (Figure 2g) confirm the presence of an additional structural domain with an interplanar spacing of 0.208 nm, corresponding to the (111) plane of cubic Cu. [37, 38] The metallic Cu domains are contiguous with the CuSe matrix, which retains its primary [001]-oriented hexagonal structure with an interspacing of 0.288 nm and a dihedral angle of 60°, corresponding to the (006) plane. [39] For comparison, Cu/CuSe samples with varying degrees of reduction (Cu/CuSe-5, and Cu/CuSe-50) were also prepared. For Cu/CuSe-5, SEM and TEM analyses revealed a relatively smooth surface compared to pristine CuSe, whereas HRTEM observations identified metallic Cu located at the edges of the CuSe nanosheets (Supporting Information S1: Figure S5). In contrast, Cu/CuSe-50 exhibited prominent diffraction peaks corresponding to elemental Se in XRD patterns (Supporting Information S1: Figure S4). TEM characterization revealed abundant surface particles on CuSe, with HRTEM confirming the coexistence of metallic Cu and Se within these particles (Supporting Information S1: Figure S6). Based on these structural variations, it was deduced that Cu/CuSe-5 was insufficiently reduced, whereas Cu/CuSe-50 displayed excessive reduction. Consequently, both samples were excluded from further optical property testing and photocatalytic CO_2 reduction performance evaluation.

X-ray photoelectron spectroscopy (XPS), and electron paramagnetic resonance (EPR) were then performed to gain deeper insight into the chemical composition, Se vacancy-defect nature, and surface electronic structure. As shown in Figure 3a, the high-resolution XPS spectra of Cu in CuSe are deconvoluted into two characteristics peaks at binding energies of 951.8 and 931.9 eV, corresponding to Cu $2p_{1/2}$ and Cu $2p_{3/2}$ of Cu-Se bonding, respectively. By comparison, the Cu/CuSe sample displays two additional peaks at 933.1 and 953.6 eV, assigned to Cu-Cu bonding, and peaks at 934.5 and 955.5 eV, attributed to Cu-O. [40–43] These observations indicate the partial reduction of Cu^{2+} in CuSe to metallic Cu, which agrees with the HRTEM results. Two fitted peaks located at around 54.7 and 53.8 eV can be attributed to Se $3d_{3/2}$ and Se $3d_{5/2}$ of Se^{2-} for Cu/CuSe (Figure 3b). [44] Notably, these peaks are slightly shifted to lower binding energies than those of pristine CuSe (54.8 and 53.9 eV, respectively). This shift in Cu/CuSe implies a lower coordination environment of Se atoms and the existence of Se vacancies. This inference is also validated by ESR (Figure 3c), where a stronger EPR signal with a calculated g value of 2.02 can be attributed to Se vacancies-induced trapping of unpaired electrons [45].

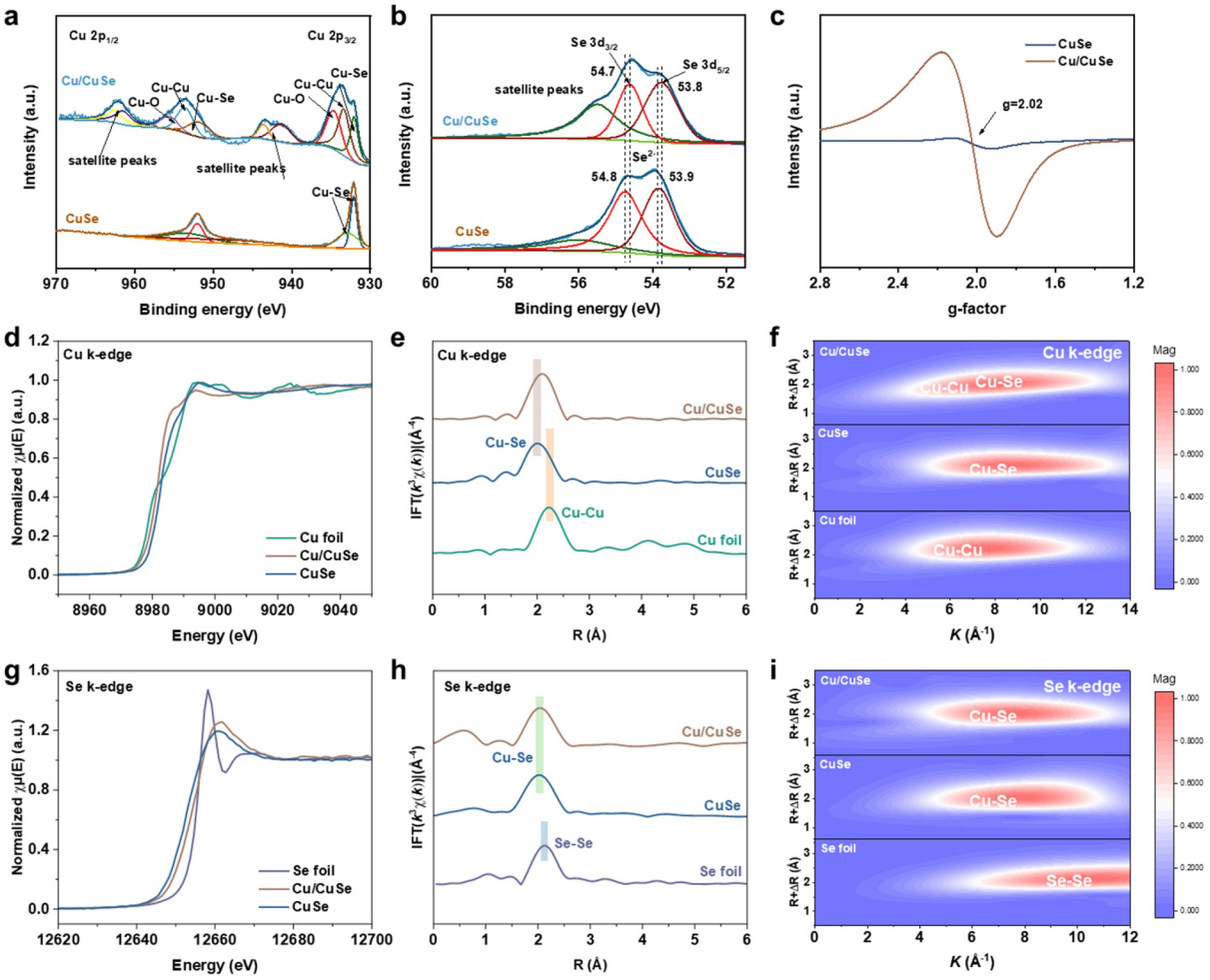

FIGURE 3 | High-resolution XPS spectra of Cu 2p (a) and Se 3d (b) for Cu/CuSe and CuSe. (c) EPR of Cu/CuSe and CuSe. Normalized XANES spectra (d) and EXFAS curves (e) of the Cu K-edge for Cu/CuSe and CuSe. (f) WT for the FT k^3-weighted χ(k)-function of Cu/CuSe and reference samples at the Cu K-edges. Normalized XANES spectra (g) and EXFAS curves (h) of the Se K-edge for Cu/CuSe and CuSe. (i) WT for the FT k^3-weighted χ(k)-function of Cu/CuSe and reference samples at the Se K-edges.

Synchrotron-based X-ray absorption spectroscopy (XAS) was further employed to investigate the electronic structure and atomic coordination environment of Cu and Se species. The Cu K-edge X-ray absorption near-edge structure (XANES) spectra reveal a pronounced shift of the absorption edge toward lower energy in Cu/CuSe compared to CuSe (Figure 3d), indicating that the introduction of heterojunctions and Se vacancies induces charge redistribution at the Cu atomic interface, leading to a reduced oxidation state of Cu. Fourier transform extended X-ray absorption fine structure (FT-EXAFS) analysis at the Cu K-edge demonstrates that the dominant peak of CuSe at 2.02 Å corresponds to the first coordination shell of Cu-Se (Figure 3e). In contrast, Cu/CuSe displays a primary peak at 2.09 Å, intermediate between the bond lengths of Cu-Se (2.02 Å) and Cu-Cu (2.18 Å), confirming the coexistence of both bonding configurations. Our combined XPS and XAS analyses provide robust and complementary evidence for the presence of Cu^0 species in the Cu/CuSe heterostructure. Quantitative EXAFS curve-fitting results further indicate that the coordination environment of Cu in Cu/CuSe comprises both Cu-Cu and Cu-Se scattering paths (Supporting Information S1: Figure S7), whereas CuSe exhibits only the characteristic Cu-Se coordination. Furthermore, the reduced peak intensity in the *R*-space for the first coordination shell of Cu/CuSe compared to CuSe reflects increased atomic disorder, which further suggests a reduced number of Se-coordinating atoms. The combination of elemental analysis and EPR results substantiates the presence of Se vacancies in the Cu/CuSe structure. Wavelet transform (WT) EXAFS contour plots display a maximum intensity for Cu-Se bonds in CuSe at $k = 8.5$ Å^{-1}, whereas Cu/CuSe exhibits a pronounced intensity shift toward the Cu-Cu bonding region (Figure 3f). These findings collectively demonstrate that the local coordination environment and electronic configuration of Cu atoms in Cu/CuSe are synergistically modulated by Se vacancies and the dense heterointerface.

Se K-edge XANES analysis demonstrates that the absorption threshold energy of Cu/CuSe lies between those of Se foil and CuSe (Figure 3g), confirming a significantly higher valence state of Se in Cu/CuSe compared to CuSe. Se K-edge FT-EXAFS spectra at the Se K-edge reveal a dominant peak at 2.02 Å in Cu/CuSe (Figure 3h), corresponding to the first coordination shell of Se-Cu bonds. Notably, no characteristic peak associated with Se-Se bonds (typically at 2.12 Å) is detected, consistent with the coordination pattern observed in CuSe. Quantitative EXAFS fitting analysis further indicates that the coordination number

(CN = 2.6) of Se in Cu/CuSe is markedly lower than that in CuSe (CN = 3.2), directly confirming the presence of selenium vacancy defects in the basal plane of Cu/CuSe nanosheets (Supporting Information S1: Figure S8 and Table S1). WT-EXAFS contour plots exhibit a maximum intensity peak at $k \approx 7.8$ Å^{-1} for Cu-Se bonds in Cu/CuSe (Figure 3i), whereas no Se-Se coordination signal is observed. These findings collectively demonstrate that the synergistic interplay between Se vacancies and Cu-Se interactions in Cu/CuSe effectively modulates the local electronic structure and coordination environment of Cu atoms, thereby regulating defect-induced interfacial charge dynamics and enhancing catalytic performance in heterostructured catalysts.

The modified band structure and light capturing properties of Cu/CuSe, influenced by Se vacancies and metallic Cu, were evaluated using ultraviolet–visible diffuse reflectance spectra (UV-vis DRS) (Figure 4a). In the visible light region, a red shift in the absorption edge from ~579 nm of CuSe to 600 nm is observed for the Cu/CuSe sample. This corresponds to a slight narrowing of the bandgap from 2.17 eV (CuSe) to 2.07 eV (Cu/CuSe), as calculated using the Kubelka–Munk approach. The subtle change in bandgap indicates an insignificant influence of the reduction on the CuSe crystal phase in Cu/CuSe in comparison with pristine CuSe. Thus, the photoredox energy potential of CuSe is well preserved in Cu/CuSe. Strikingly, Cu/CuSe shows strong visible–NIR light absorption beyond the original plasmonic resonance wavelength of ~940 nm, manifesting an extended light harvesting ability. This extension is primarily attributed to the altered localized surface electronic structure, which induces plasmonic resonances at diverse wavelengths. Meanwhile, the formation of internal defect states associated with Se vacancies introduce new energy levels, contributing to extra light absorption. Collectively, these effects facilitate an enhanced solar energy utilization-assisted photochemical–photothermal synergy.

To assess the photochemical properties, the conduction bands (CB) were characterized using Mott–Schottky plots at different frequencies. As presented in Supporting Information S1: Figure S9, n-type semiconductor characteristics of both Cu/CuSe and CuSe can be confirmed by the negative slopes and X-intercepts. The CBs positions were measured to be −0.62 and −0.60 eV for Cu/CuSe and CuSe, respectively, confirming that the negative potential of photoexcited electrons is retained in Cu/CuSe. In parallel with the optical analysis, the potential energies of the valence band (VB) are summarized in a schematic diagram (Figure 4b). Theoretically, the potentials of CBs and VBs are sufficiently energetic to drive CO_2 reduction and water oxidization simultaneously. Subsequently, steady-state room-

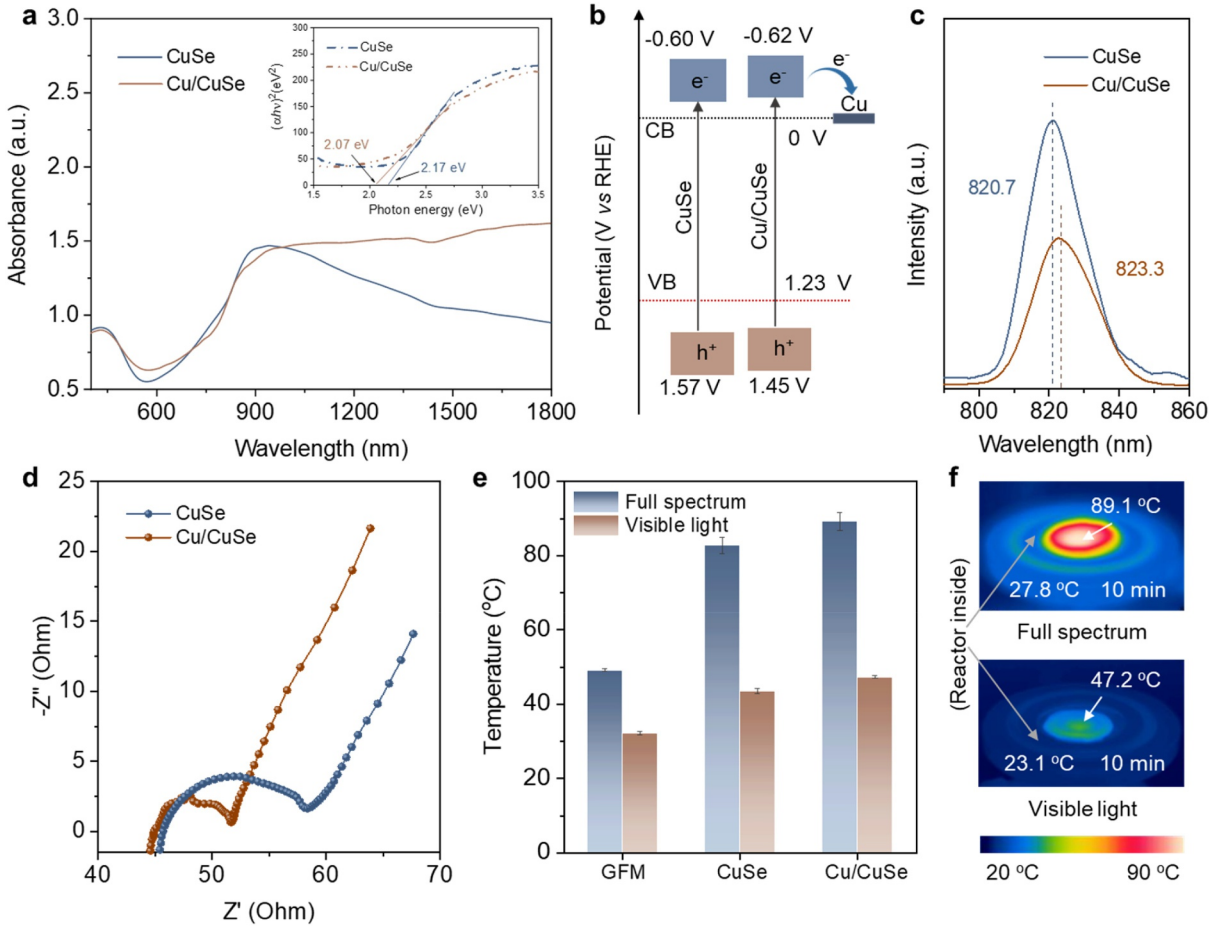

FIGURE 4 | UV–vis–NIR absorption spectra (a), schematic of the potential energy diagram (b), fluorescence spectra (c), Nyquist plots (d) of Cu/CuSe and CuSe. (e) Photothermal temperature of glass fiber membrane (GFM), Cu/CuSe and CuSe under visible light and full spectrum. (f) FLIR images of Cu/CuSe photocatalytic membrane and pure GFM.

temperature fluorescence (FL) spectrum and photo/electrochemical (PE) characterizations were performed to investigate photoexcited electron–hole pairs and separation-transfer efficiency. In the FL spectra (Figure 4c), Cu/CuSe exhibits a broad emission peak around 825 nm, accompanied by a slight shift from the band gap emission and an observable decrease in FL intensity compared to the pristine CuSe. This unambiguously demonstrates that metallic Cu and interband states introduced by Se vacancies accelerate the separation of photoexcited electron–hole pairs and dramatically reduce charge recombination. Regarding PE performance, the transient photocurrent responses under simulated solar irradiation are determined to be 0.26 and 0.15 $\mu A/cm^{-2}$ for Cu/CuSe and CuSe, respectively (Supporting Information S1: Figure S10). Additionally, electrochemical impedance spectroscopy (EIS) analysis of Cu/CuSe shows a smaller semicircle radius than that of CuSe (Figure 4d), suggesting lower interfacial charge transfer resistance. The contrasting higher photocurrent density and lower charge-transfer resistance of Cu/CuSe reaffirm the crucial role of metallic Cu and Se vacancies toward suppressed electron–hole recombination and augmented charge transport kinetics.

To evaluate the photothermal conversion performance, the temperature profiles and infrared images of Cu/CuSe and CuSe were recorded under simulated one sun irradiation (100 mW cm^{-2}). As shown in Figure 4e,f and Supporting Information S1: Figure S11, the temperature of Cu/CuSe rapidly rises from 22°C to 89.1°C in 10 min, which is notably higher than that of CuSe (82.1°C). To a large extent, this is due to the enhanced NIR photo-to-thermal conversion (for wavelength exceeding 940 nm) (Supporting Information S1: Figure S12) of Cu/CuSe, taking into consideration the similar morphological structure-induced reflection of incident light by both samples.

The performance of photocatalytic CO_2 reduction is investigated to validate its concerted photochemical–photothermal mechanism. Measurements were conducted in a gas–solid reactor under simulated one sun irradiation without any sacrificial reagents or photosensitizers. Water vapor provides a proton source and participates in the complementary oxidation reaction. $Ni(OH)_2$ (Supporting Information S1: Figures S13–15) was incorporated with Cu/CuSe as a co-catalyst to facilitate the water oxidation half-reaction. Specifically, it acts as a hole acceptor, promoting the separation of photogenerated charge carriers and providing protons for the reduction reaction. [46] This synergy leads to an enhanced overall photocatalytic efficiency, as verified by the optimal performance at a 1:1 ratio (Supporting Information S1: Figure S16). Gas chromatography (GC) and liquid ^1H NMR were employed to detect the presence of gas and liquid products, respectively. As shown in Supporting Information S1: Figure S17, only gaseous products of CO and H_2 without liquid products can be detected in the presence of photocatalysts, CO_2, and vapor under light irradiation. In order to further ascertain the reduction of CO_2 molecules, $^{13}CO_2$ and $H_2{}^{18}O$ isotopic labeling experiments were performed (Supporting Information S1: Figure S18). The detection of a peaks at m/z values of 29 (^{13}CO) confirm that the carbon source of CO originates from the photoreduction of CO_2 molecule. Simultaneously, peaks at m/z values of 34 ($^{16}O^{18}O$) and 36 ($^{18}O_2$) verify that O_2 was produced from water oxidation. Thus, the production rates are linearly dependent on the reduced CO_2 molar quantity in the reaction process. As shown in Figure 5a, Cu/CuSe achieves a CO production rate of 27.06 $\mu mol\ g^{-1}\ h^{-1}$, and H_2 of 3.04 $\mu mol\ g^{-1}\ h^{-1}$ under simulated solar irradiation, higher than that of CuSe (CO 9.42 $\mu mol\ g^{-1}\ h^{-1}$, H_2 2.41 $\mu mol\ g^{-1}\ h^{-1}$). Moreover, Cu/CuSe exhibits enhanced photoactivity under either individual UV or visible irradiation compared to CuSe (Figure 5b). In view of almost identical absorption profiles of CuSe and Cu/CuSe in the UV–vis region and similar CB potentials, the abundance of active centers for CO_2 conversion becomes critical for the reaction rate. The main differences between these materials pertain to the presence of nested metallic Cu clusters and Se vacancies in Cu/CuSe. As previously reported, Cu-based catalysts are well known as highly active catalysts for CO_2 reduction, where modulation of their oxidation states can further lower the activation energy and accelerate the reaction under the same potential.

To investigate the influence of solar–thermal heating on CO_2 photoreduction, the production rates of CO and H_2 under various selective or combinatorial wavelength were tested. Under monochromatic high-wavelength irradiation, only hydrogen evolution was observed, with no detectable CO_2 reduction product. Specifically, H_2 generation rates are 1.05 and 1.29 $\mu mol\ g^{-1}\ h^{-1}$ for the respective wavelength of 850 and 950 nm (Figure 5b). This implies that LSPR hot electrons, originating from the intrinsic plasmonic semiconductor properties of CuSe, can induce H_2 evolution photoactivity but are not energetic enough to dissociate CO_2 molecules. Conversely, the introduction of an additional 850 or 950 nm monochromatic light to the visible light resulted in simultaneous production of both CO and H_2 production. Unlike H_2 generation, which can be directly driven by LSPR hot electrons, CO_2 reduction to CO mainly benefits from the plasmon-induced photothermal effect. This heat improves the kinetic energy of photogenerated electron–hole pairs to accelerate the mobility of charge carriers and inhibit their recombination. Consequently, enhanced photocatalytic performance is achieved. [35] As expected, the higher efficiency of LSPR hot electrons for H_2 evolution leads to a slight decrease in selectivity toward CO_2 reduction products (Figure 5c). However, a higher proportion of photothermic heating across the whole NIR region improves the CO selectivity from 82.27% (vis) to over 90% (full spectrum). Notably, the CO production rate and selectivity of our $Cu/CuSe/Ni(OH)_2$ system are competitive with other advanced photocatalysts reported recently (Supporting Information S1: Table S3). In addition, Cu/CuSe demonstrates high photocatalytic recyclability and physicochemical stability over consecutive cycles (Figure 5d). Collectively, well-preserved morphology, stable crystal structure, and surface chemical states are evident from the SEM images, element mapping, and XPS spectra after a long-term photocatalytic process (Supporting Information S1: Figures S19 and S20). Notably, although the Se 3d XPS satellite peak exhibits a slight upward shift in binding energy, likely due to surface adsorption of reaction intermediates or minor oxidation under operational conditions, the post-reaction XRD analysis

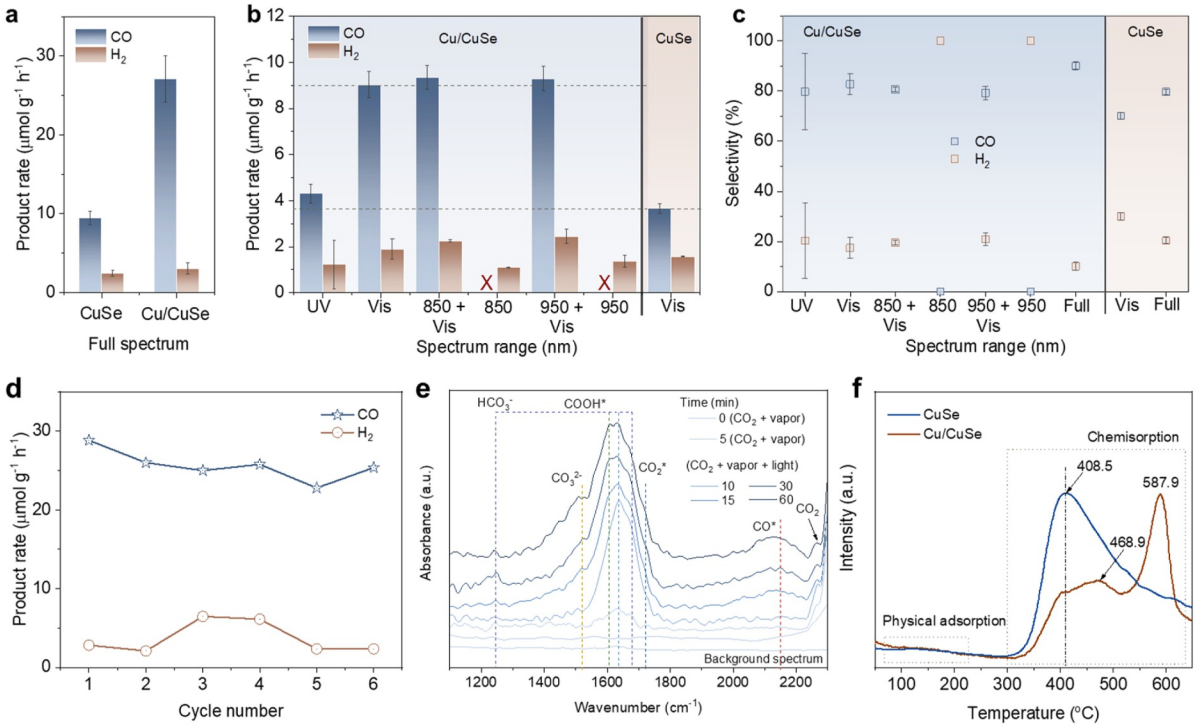

FIGURE 5 | Photocatalytic CO_2-reduction activity of Cu/CuSe and CuSe under full spectrum (a), and various radiation types (b). (c) CO and H_2 product selectivity. (d) Cyclic measurements of CO_2 photoreduction over Cu/CuSe. (e) In situ DRIFTS spectra for the CO_2 photocatalytic reduction process over Cu/CuSe. (f) CO_2-TPD spectra of Cu/CuSe and CuSe.

unambiguously shows that the crystalline structure of Cu/CuSe remains well preserved, affirming the robust stability of the catalyst (Supporting Information S1: Figure S21).

In situ diffuse reflectance infrared Fourier transformed spectroscopy (DRIFTS) measurements were performed to uncover the CO_2 reduction process through real-time monitoring of the reaction intermediates. Prior to the reaction, a background spectrum was collected under pure Ar flow after purging the catalyst and was subtracted from all subsequent spectra. Figure 5e presents FTIR curves recorded over time, where several distinct peaks corresponding to various intermediate species progressively emerge upon injecting moist CO_2 gas flow and introduction of light illumination. The 0 min spectrum designates the background collected under the CO_2 and H_2O vapor atmosphere before illumination. Following this background measurement, CO_2 initially adsorbs on the Cu/CuSe catalyst surface, followed by the appearance of correlative characteristic peaks associated with reaction intermediates. The peaks at 1519 and 1725 cm^{-1} are assigned to the symmetric O-C-O stretches of CO_3^{2-} and CO_2* groups, respectively. The peaks at 1247, 1635, and 1677 cm^{-1} match the vibration frequency of HCO_3^-, formed upon CO_2 and H_2O co-adsorption. The peaks at 1605 and 2149 cm^{-1} are ascribed to the stretching vibrations of COOH* and CO* groups. Significantly, their intensities gradually increase with prolonged light irradiation, suggesting their pivotal roles as intermediates for continuous photoreduction of CO_2 into CO.

To further probe the CO_2 adsorption behaviors and identify possible reduction pathways, CO_2 temperature-programmed desorption (TPD) was conducted. The corresponding CO_2-TPD profiles can be divided into two regions: physisorption and chemisorption (Figure 5f). A broad desorption peak at low-temperature around 140°C is associated to physical adsorption CO_2, with Cu/CuSe showing greater intensity due to its larger specific surface area. A moderate desorption peak at approximately 408.5°C is related to CO_2 desorption from lattice Se anions in CuSe, whereas a higher desorption peak at ~468.9°C is attributed to presence of Se vacancies. Furthermore, a higher-temperature desorption peak at 587.9°C demonstrates a stronger ability of Cu/CuSe to capture CO_2, which can be attributed to embedded metallic Cu. Consequently, a possible photocatalytic CO_2 reduction pathway is proposed. In brief, CO_2 molecules adsorb onto metallic Cu catalytic sites, forming stable CO_2*, whereas H_2O dissociates into hydroxyl and protons. Soon afterward, injection of photogenerated electrons from CuSe react with CO_2* and surface protons to generate carboxyl (COOH*) radicals, which are further protonated into CO* intermediates. The desorption of CO* leads to the release of gaseous CO from active sites after the CO* desorption. In this process, photogenerated holes drive the hydroxyl oxidation reaction, as reflected by GS-MS results (Supporting Information S1: Figure S18). Additionally, unstable CO_2* reacts with hydroxyl to form CO_3^{2-} or HCO_3^- absorbed on the surface of photocatalyst, as confirmed by in situ DRIFTS. Taken together, photothermal heating and the incorporation of metallic Cu remarkably enhances the efficiency of CO_2 photoreduction.

The proposed reaction mechanism is confirmed using density functional (DFT) calculations of CO_2 reduction reaction on Cu (111), CuSe(001) slab, as well as CuSe support with embedded Cu nanoparticles. The latter model comprises a 119-atom Cu nanoparticle (NP) interfaced with a four-layer p(7 × 7) CuSe

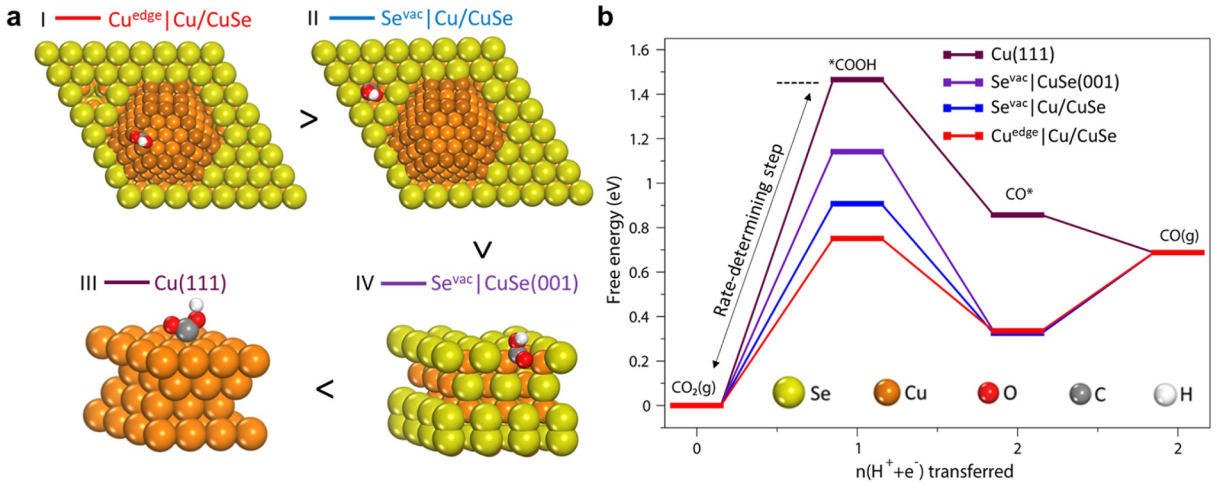

FIGURE 6 | DFT calculations of CO_2RR on Cu and CuSe-based catalyst surfaces. (a) Ranking of the considered catalyst model (with displayed *COOH intermediate) from the most active to the least active in CO_2 reduction. The atomic colors are as follows: bronze (Cu), lime-green (Se), red (O), gray (C), and white (H). (b) Free energy diagram illustrating the CO_2 reduction pathway on the catalytic surfaces, showing the energy profiles for key intermediates (*COOH) and products (*CO), consistent with their catalytic activities. Note that adsorption energies of *CO happen to be very similar on all considered catalysts besides Cu(111).

(001) slab with geometry obtained through systematic scanning (Supporting Information S1: Figure S22). In this embedded configuration, the Cu NP partially integrates into the Se-deficient CuSe surface, mimicking realistic experimental conditions. In particular, this model represents well the electron transfer between Cu and CuSe (Supporting Information S1: Table S2), the polarization of electron density at their interface, as well as the emergence of new electronic states (Supporting Information S1: Figures S23 and S24).

The free energy profiles of CO_2 reduction presented in Figure 6 and Supporting Information S1: Figure S25 constructed based on the analysis of various binding sites on the considered models (Supporting Information S1: Figure S26) reveal that the formation of the *COOH intermediate is the most challenging reaction step in all cases. On Cu(111), the free energy barrier for *COOH formation reaches 1.48 eV, indicating sluggish reaction kinetics and limited catalytic activity. In contrast, introducing Se-vacancy on CuSe surface (Se^{vac} | CuSe(001)) significantly reduces the energy barrier to 1.16 eV, demonstrating improved catalytic performance. Further enhancement is observed when a Cu nanoparticle is embedded into CuSe (Se^{vac} | Cu/CuSe), where the energy barrier is reduced to 0.89 eV. Notably, the most striking improvement is observed at the Cu nanoparticle edge site (Cu^{edge} | Cu/CuSe), which exhibits the lowest *COOH formation barrier of just 0.72 eV—a ~50% reduction compared to Cu(111), facilitating a highly efficient reaction pathway.

These findings underscore the pivotal role of Cu NP edge sites and their interaction with the CuSe support in enhancing catalytic performance for CO_2 reduction. The embedding of Cu NPs creates an interface structure that stabilizes intermediates, lowers energy barriers, and facilitates charge transfer, ultimately improving both activity and efficiency of CO_2 reduction. In addition to optimizing CO_2RR, this study provides a generalized strategy for designing advanced catalysts. The principles demonstrated here can be extended to other metal-chalcogenide systems, where structural modifications, such as embedding nanoparticles or tuning interface properties, can further enhance catalytic performance for various reactions.

3 | Conclusion

In summary, we have demonstrated a photochemical–photothermal synergistic catalyst in the form of nested Cu/CuSe heterostructure for efficient CO_2 photoreduction. The Se vacancies and in-plate metallic Cu clusters within CuSe nanosheets extends photothermal conversion beyond the intrinsic plasmonic wavelength of CuSe and establishes robust catalytically active sites. Our study reveals the key contributions of in-plane metallic Cu clusters in promoting CO_2 adsorption and lowering the activation energy of the rate-determining step in the succedent conversion pathway. Simultaneously, Se vacancies introduce new gap states that broaden IR-light absorption. Accordingly, these synergistic effects result in a threefold improvement in CO production rate under full-spectrum solar irradiation. This work pioneers a feasible way to expand light-response with intact plasmonic effect in the IR region of plasmonic semiconductor to facilitate photocatalytic reactions toward effective solar harvesting and utilization.

Acknowledgments

We acknowledge financial support from the A*STAR under its RIE2025 Manufacturing, Trade and Connectivity (MTC award M22K2c0081) and Individual Research Grant (IRG award M23M6c0105) as well as the National University of Singapore (WBS A-0009169-01-00), National Natural Science Foundation of China (22579154, 52202319), Natural Science Foundation of Shandong (2022HWYQ-062), Shandong TaiShan Scholars (tsqn202211066), and Fundamental Research Funds for the Central Universities (202461108).

Conflicts of Interest

The authors declare no conflicts of interest.

Data Availability Statement

The data that support the findings of this study are available from the corresponding author upon reasonable request.

References

1. M. Bonchio, J. Bonin, O. Ishitani, et al., "Best Practices for Experiments and Reporting in Photocatalytic CO_2 Reduction," *Nature catalysis* 6, no. 8 (2023): 657–665, https://doi.org/10.1038/s41929-023-00992-7.

2. A. Wagner, C. D. Sahm, and E. Reisner, "Towards Molecular Understanding of Local Chemical Environment Effects in Electro- and Photocatalytic CO_2 Reduction," *Nature catalysis* 3, no. 10 (2020): 775–786, https://doi.org/10.1038/s41929-020-00512-x.

3. D. Li, M. Kassymova, X. Cai, S.-Q. Zang, and H.-L. Jiang, "Photocatalytic CO_2 Reduction Over Metal-Organic Framework-Based Materials," *Coordination Chemistry Reviews* 412 (2020): 213262, https://doi.org/10.1016/j.ccr.2020.213262.

4. H. Kumagai, Y. Tamaki, and O. Ishitani, "Photocatalytic Systems for CO_2 Reduction: Metal-Complex Photocatalysts and Their Hybrids With Photofunctional Solid Materials," *Accounts of Chemical Research* 55, no. 7 (2022): 978–990, https://doi.org/10.1021/acs.accounts.1c00705.

5. H. Takeda, K. Ohashi, A. Sekine, and O. Ishitani, "Photocatalytic CO_2 Reduction Using Cu(I) Photosensitizers With a Fe(II) Catalyst," *Journal of the American Chemical Society* 138, no. 13 (2016): 4354–4357, https://doi.org/10.1021/jacs.6b01970.

6. G. Wang, Z. Chen, T. Wang, D. Wang, and J. Mao, "P and Cu Dual Sites on Graphitic Carbon Nitride for Photocatalytic CO_2Reduction to Hydrocarbon Fuels With High C_2H_6Evolution," *Angewandte Chemie International Edition* 61, no. 40 (2022): e202210789, https://doi.org/10.1002/anie.202210789.

7. M. Zhou, Z. Wang, A. Mei, et al., "Photocatalytic CO_2 Reduction Using La-Ni Bimetallic Sites Within a Covalent Organic Framework," *Nature Communications* 14, no. 1 (2023): 2473, https://doi.org/10.1038/s41467-023-37545-2.

8. J. Wang, W. Zhu, F. Meng, G. Bai, Q. Zhang, and X. Lan, "Integrating Dual-Metal Sites Into Covalent Organic Frameworks for Enhanced Photocatalytic CO_2 Reduction," *ACS Catalysis* 13, no. 7 (2023): 4316–4329, https://doi.org/10.1021/acscatal.3c00126.

9. H. Huang, R. Shi, Z. Li, J. Zhao, C. Su, and T. Zhang, "Triphase photocatalytic CO_2 reduction over silver-decorated titanium oxide at a gas–water boundary," *Angewandte Chemie* 134 (2022): e202200802, https://doi.org/10.1002/ange.202200802.

10. X. Li, L. Li, G. Chen, et al., "Accessing Parity-Forbidden d-d Transitions for Photocatalytic CO_2 Reduction Driven by Infrared Light," *Nature Communications* 14, no. 1 (2023): 4034, https://doi.org/10.1038/s41467-023-39666-0.

11. W. Song, K. C. Chong, G. Qi, et al., "Unraveling the Transformation From Type-II to Z-Scheme in Perovskite-Based Heterostructures for Enhanced Photocatalytic CO_2 Reduction," *Journal of the American Chemical Society* 146, no. 5 (2024): 3303–3314, https://doi.org/10.1021/jacs.3c12073.

12. N. Li, X. Chen, J. Wang, et al., "ZnSe Nanorods–$CsSnCl_3$ Perovskite Heterojunction Composite for Photocatalytic CO_2 Reduction," *ACS Nano* 16, no. 2 (2022): 3332–3340, https://doi.org/10.1021/acsnano.1c11442.

13. S. Si, H. Shou, Y. Mao, et al., "Low-Coordination Single Au Atoms on Ultrathin $ZnIn_2S_4$Nanosheets for Selective Photocatalytic CO_2Reduction Towards CH_4," *Angewandte Chemie International Edition* 61, no. 41 (2022): e202209446, https://doi.org/10.1002/anie.202209446.

14. X. Liu, T. Chen, Y. Xue, et al., "Nanoarchitectonics of MXene/semiconductor Heterojunctions Toward Artificial Photosynthesis via Photocatalytic CO_2 Reduction," *Coordination Chemistry Reviews* 459 (2022): 214440, https://doi.org/10.1016/j.ccr.2022.214440.

15. W. Shangguan, Q. Liu, Y. Wang, et al., "Molecular-Level Insight into Photocatalytic CO_2 Reduction With H_2O over Au Nanoparticles by Interband Transitions," *Nature Communications* 13, no. 1 (2022): 3894, https://doi.org/10.1038/s41467-022-31474-2.

16. X. Jiang, J. Huang, Z. Bi, et al., "Plasmonic Active 'Hot Spots'-Confined Photocatalytic CO_2 Reduction With High Selectivity for CH_4 Production," *Advanced Materials* 34, no. 14 (2022): 2109330, https://doi.org/10.1002/adma.202109330.

17. Y. Huang, K. Dai, J. Zhang, and G. Dawson, "Photocatalytic CO_2 Conversion of $W_{18}O_{49}$/CdSe-Diethylenetriamine With High Charge Transfer Efficiency: Synergistic Effect of LSPR Effect and S-Scheme Heterojunction," *Chinese Journal of Catalysis* 43, no. 10 (2022): 2539–2547, https://doi.org/10.1016/s1872-2067(21)64024-x.

18. J. Jiang, X. Wang, and H. Guo, "Enhanced Interfacial Charge Transfer/Separation by Lspr-Induced Defective Semiconductor Toward High Co_2RR Performance," *Small* 19, no. 33 (2023): 2301280, https://doi.org/10.1002/smll.202301280.

19. Q. Zhu, Y. Xuan, K. Zhang, and K. Chang, "Enhancing Photocatalytic CO_2 Reduction Performance of g-C3N4-based Catalysts With Non-Noble Plasmonic Nanoparticles," *Applied Catalysis B: Environmental* 297 (2021): 120440, https://doi.org/10.1016/j.apcatb.2021.120440.

20. R. Verma, R. Belgamwar, and V. Polshettiwar, "Plasmonic Photocatalysis for CO_2 Conversion to Chemicals and Fuels," *ACS Materials Letters* 3, no. 5 (2021): 574–598, https://doi.org/10.1021/acsmaterialslett.1c00081.

21. Y. Li, Y. Lei, D. Li, et al., "Recent Progress on Photocatalytic CO_2 Conversion Reactions over Plasmonic Metal-Based Catalysts," *ACS Catalysis* 13, no. 15 (2023): 10177–10204, https://doi.org/10.1021/acscatal.3c02550.

22. D. Devasia, A. J. Wilson, J. Heo, V. Mohan, and P. K. Jain, "A Rich Catalog of C–C Bonded Species Formed in CO2 Reduction on a Plasmonic Photocatalyst," *Nature Communications* 12, no. 1 (2021): 2612, https://doi.org/10.1038/s41467-021-22868-9.

23. Z. Zhu, R. Tang, C. Li, X. An, and L. He, "Promises of Plasmonic Antenna-Reactor Systems in Gas-Phase CO2 Photocatalysis," *Advanced Science* 10 (2023): 2302568, https://doi.org/10.1002/advs.202302568.

24. S. Luo, X. Ren, H. Lin, H. Song, and J. Ye, "Plasmonic Photothermal Catalysis for Solar-To-Fuel Conversion: Current Status and Prospects," *Chemical Science* 12, no. 16 (2021): 5701–5719, https://doi.org/10.1039/d1sc00064k.

25. F. Zhang, Y.-H. Li, M.-Y. Qi, et al., "Photothermal Catalytic CO_2 Reduction over Nanomaterials," *Chem Catalysis* 1, no. 2 (2021): 272–297, https://doi.org/10.1016/j.checat.2021.01.003.

26. C. Xu, X. Zhang, M.-N. Zhu, et al., "Accelerating Photoelectric CO_2 Conversion With a Photothermal Wavelength-Dependent Plasmonic Local Field," *Applied Catalysis B: Environmental* 298 (2021): 120533, https://doi.org/10.1016/j.apcatb.2021.120533.

27. J. Zhou, H. Liu, and H. Wang, "Photothermal Catalysis for CO_2 Conversion," *Chinese Chemical Letters* 34, no. 2 (2023): 107420, https://doi.org/10.1016/j.cclet.2022.04.018.

28. S. Du, G. Li, X. Lin, S. Zhang, H. Xu, and P. Fang, "Highly Efficient H_2 Generation Over Cu2Se Decorated CdS0.95Se0.05 Nanowires by Photocatalytic Water Reduction," *Chemical Engineering Journal* 409 (2021): 128157, https://doi.org/10.1016/j.cej.2020.128157.

29. C. Yang, M. Wang, M. Chang, et al., "Heterostructural Nanoadjuvant CuSe/$CoSe_2$ for Potentiating Ferroptosis and Photoimmunotherapy Through Intratumoral Blocked Lactate Efflux," *Journal of the American Chemical Society* 145, no. 13 (2023): 7205–7217, https://doi.org/10.1021/jacs.2c12772.

30. S.-L. Gong, Y. Tian, G.-P. Sheng, and L.-J. Tian, "Dual-Mode Harvest Solar Energy for Photothermal Cu2-xSe Biomineralization and

Seawater Desalination by Biotic-Abiotic Hybrid," *Nature Communications* 15, no. 1 (2024): 4365, https://doi.org/10.1038/s41467-024-48660-z.

31. X. Luan, Y. Pan, Y. Zhou, et al., "Targeted Self-Assembly of Renal Clearable $Cu_{2-x}Se$ to Induce Lysosome Swelling for Multimodal Imaging Guided Photothermal/Chemodynamic Synergistic Therapy," *Advanced Functional Materials* 32, no. 51 (2022): 2208354, https://doi.org/10.1002/adfm.202208354.

32. J. Wang, H. Zhang, Y. Nian, et al., "Disruption Symmetric Crystal Structure Favoring Photocatalytic CO_2 Reduction: Reduced *COOH Formation Energy Barrier on Al Doped CuS/TiO_2," *Advanced Functional Materials* 34, no. 42 (2024): 2406549, https://doi.org/10.1002/adfm.202406549.

33. Z. Yu, X. Luan, H. Xiao, et al., "Gemstone Nanoflower-Shaped $ZnIn_2S_4$/CuS Heterojunction With Ultralong Lifetime of Photoinduced Carriers for Photocatalytic Hydrogen Evolution," *Applied Catalysis B: Environment and Energy* 347 (2024): 123702, https://doi.org/10.1016/j.apcatb.2024.123702.

34. D. Chen, Y. Xu, J. Lu, et al., "Intercalation-Induced Localized Conversion Reaction in *H-Cus*e for Ultrafast-Rechargeable and Long-Cycling Sodium Metal Battery," *Advanced Materials* 36, no. 32 (2024): 2404640, https://doi.org/10.1002/adma.202404640.

35. X. Gong, S. Fan, Q. Yang, et al., "Porous Two-Dimensional Cuse@Bioi Isotype Heterojunction With Highly Exposed (1 0 2) Facets for Efficient Photoelectrocatalytic CO_2 Reduction and Photodetection," *Chemical Engineering Journal* 493 (2024): 152773, https://doi.org/10.1016/j.cej.2024.152773.

36. M. Sajjad, M. Z. U. Shah, M. S. Javed, et al., "A Novel High-Performance All-Solid-State Asymmetric Supercapacitor Based on CuSe Nanoflakes Wrapped on Vertically Aligned TiO2 Nanoplates Nanocomposite Synthesized via a Wet-Chemical Method," *Journal of Energy Storage* 55 (2022): 105304, https://doi.org/10.1016/j.est.2022.105304.

37. Q. Fan, X. Zhang, X. Ge, et al., "Manipulating Cu Nanoparticle Surface Oxidation States Tunes Catalytic Selectivity Toward CH_4 or C_{2+} Products in CO_2 Electroreduction," *Advanced Energy Materials* 11, no. 36 (2021): 2101424, https://doi.org/10.1002/aenm.202101424.

38. I. Roh, S. Yu, C.-K. Lin, S. Louisia, S. Cestellos-Blanco, and P. Yang, "Photoelectrochemical CO_2 Reduction Toward Multicarbon Products With Silicon Nanowire Photocathodes Interfaced With Copper Nanoparticles," *Journal of the American Chemical Society* 144, no. 18 (2022): 8002–8006, https://doi.org/10.1021/jacs.2c03702.

39. X. J. Wu, X. Huang, J. Liu, et al., "Two-Dimensional CuSe Nanosheets With Microscale Lateral Size: Synthesis and Template-Assisted Phase Transformation," *Angewandte Chemie International Edition* 53, no. 20 (2014): 5083–5087, https://doi.org/10.1002/anie.201311309.

40. C. Chen, J. Zhang, X. Xiong, S. Yang, and J. Lin, "High Photo-Electrochemical and Hydrogen Evolution Reaction Activities From 0D/2D ZnSe/(001)CuSe Heterojunction Catalysts Constructed by ZnSe Nanoparticles and {001} Facets-Exposed CuSe Nanosheets," *ACS Applied Energy Materials* 5, no. 7 (2022): 8952–8962, https://doi.org/10.1021/acsaem.2c01443.

41. G. Li, M. Kou, J. Tu, Y. Luo, M. Wang, and S. Jiao, "Coordination Interaction Boosts Energy Storage in Rechargeable Al Battery With a Positive Electrode Material of CuSe," *Chemical Engineering Journal* 421 (2021): 127792, https://doi.org/10.1016/j.cej.2020.127792.

42. Y. Yang, J. Xiao, J. Cai, et al., "Mixed-Valence Copper Selenide as an Anode for Ultralong Lifespan Rocking-Chair Zn-Ion Batteries: An Insight Into Its Intercalation/Extraction Kinetics and Charge Storage Mechanism," *Advanced Functional Materials* 31, no. 3 (2021): 2005092, https://doi.org/10.1002/adfm.202005092.

43. C. Du, Y. Zhu, Y. Zhang, et al., "Cu+ Redox Activation and Polyselenide Stabilization via Strong Se-C Interaction for Superior Magnesium Storage," *Energy Storage Materials* 61 (2023): 102863, https://doi.org/10.1016/j.ensm.2023.102863.

44. Y. Wang, B. Wang, J. Zhang, D. Chao, J. Ni, and L. Li, "Conversion Electrochemistry of Copper Selenides for Robust and Energetic Aqueous Batteries," *Carbon Energy* 5, no. 2 (2023): e261, https://doi.org/10.1002/cey2.261.

45. X. Ma, Y. Li, X. Long, et al., "Construction of Phosphorus-Doping With Spontaneously Developed Selenium Vacancies: Inducing Superior Ion-Diffusion Kinetics in Hollow Cu2Se@C Nanospheres for Efficient Sodium Storage," *Journal of Energy Chemistry* 77 (2023): 227–238, https://doi.org/10.1016/j.jechem.2022.10.046.

46. R. Jena, V. Kashyap, R. Jana, et al., "In Situ Tracking of Ni-Mof Reconstruction Into Active Ni(OH) $_2$ OER Catalysts," *Angewandte Chemie, International Edition* 64, no. 38 (2025): e202510741, https://doi.org/10.1002/anie.202510741.

Supporting Information

Additional supporting information can be found online in the Supporting Information section.

Supporting Information S1: ece270041-sup-0001-suppl-data.docx.